Monatsh Chem (2009) 140:1041–1052
DOI 10.1007/s00706-009-0139-1

ORIGINAL PAPER

Microstructure and electrical properties of aluminium-substituted La(Sr)Ga(Mg)$O_{3-\delta}$-based solid electrolytes

Eduarda Gomes · Glenn C. Mather · Filipe M. Figueiredo · Fernando M. B. Marques

Received: 17 December 2008 / Accepted: 21 January 2009 / Published online: 27 March 2009
© Springer-Verlag 2009

Abstract A study of the influence of the substitution of Al for Ga in the ceramic processing and electrical properties of $La_{0.95}Sr_{0.05}Ga_{0.90-x}Al_xMg_{0.10}O_{3-\delta}$ $(0 \leq x \leq 0.3)$ solid electrolytes is presented. The materials retained orthorhombic symmetry over the entire substitution range, whereas a deviation from Vegard's law for $x > 0.20$ suggested a maximum Al solubility of $x = 0.20$. Scanning electron microscopy analysis of ceramic samples revealed that grain growth was inhibited for $x \geq 0.2$. This microstructural change was related to an apparent deterioration of mechanical properties, as suggested by room-temperature Vickers hardness measurements. Impedance spectroscopy revealed a significant degradation of the grain-boundary electrical properties for $x \geq 0.20$, whereas the bulk conductivity was enhanced for $0.10 \leq x \leq 0.15$. Oxygen-permeability measurements confirmed that the studied materials remain essentially pure ionic conductors. An ionic conductivity maximum of 0.047 S/cm at 700 °C was obtained for $x = 0.10$. The effect of aluminium in the grain-bulk ionic conductivity is discussed in terms of defect cluster models and assuming fast oxygen diffusion along domain walls.

E. Gomes
ESTG, Instituto Politécnico de Viana do Castelo,
P4900-348 Viana do Castelo, Portugal

G. C. Mather
Instituto de Cerámica y Vidrio, CSIC, Cantoblanco,
28049 Madrid, Spain

F. M. Figueiredo (✉) · F. M. B. Marques
Department of Ceramics and Glass Engineering, CICECO,
University of Aveiro, P3810-193 Aveiro, Portugal
e-mail: lebre@ua.pt

Keywords Solid electrolytes · Grain boundaries · Impedance spectroscopy · Oxides · Electrochemistry · Ceramics

Introduction

Strontium and magnesium co-substituted lanthanum gallate, commonly referred to in the literature as LSGM, is considered a viable alternative solid-state electrolyte to yttria-stabilized zirconia due its high oxide-ionic conductivity at intermediate temperature [1–3]. The thermal-expansion behaviour, chemical composition and a structure similar to that of many potential electrode and interconnect materials have also been highlighted as competitive advantages over other ionic conductors. However, LSGM materials have always proven difficult to process because of Ga volatilisation. The chemical incompatibility with known electrode materials (in particular with Ni-based cermets) and high cost of Ga appear to be additional serious drawbacks to the technological utilisation of this system [4–6].

Attempts to minimise these problems have consisted mainly of compositional modifications in order to reduce the gallium content, in particular by the partial substitution of gallium with aluminium. Literature reports on the effects of Al-containing LSGM have shown that: (1) the electrical properties deteriorate and the activation energy for ionic conduction tends to increase [7–9]; (2) the mechanical properties may be slightly improved for low aluminium contents [10]; (3) contrary to early reports, Ga volatisation in LSGM is not significantly reduced by decreasing Ga_2O_3 activity, e.g. by substituting for aluminium [11]. These conclusions, however, are based on polycrystalline ceramic samples where the reported effects on the electrical

properties are restrained to total conductivity, neglecting the role of grain boundaries.

This work presents a re-evaluation of the effects of substituting Ga for Al on the bulk and grain-boundary electrical properties of LSGM, and includes additional information on the structure, hardness, thermal expansion and ceramic microstructure.

Results and discussion

Structure

Figure 1 shows the powder X-ray diffraction (XRD) patterns obtained for various Al contents. Those patterns corresponding to $x < 0.20$ are free of any trace of secondary/impurity phases and could be indexed in the orthorhombic Pnma space group of the parent LSGM compound, as found for $La_{0.9}Sr_{0.1}Ga_{0.9-x}Al_xMg_{0.1}O_{3-\delta}$ [7], $La_{0.9}Sr_{0.1}Ga_{0.8-x}Al_xMg_{0.2}O_{3-\delta}$ [11] and $LaGa_{0.9-x}Al_xMg_{0.1}O_{3-\delta}$ [9]. Low-intensity diffraction maxima corresponding to unidentified secondary phase(s) were observed in all XRD patterns for $x \geq 0.20$. These additional reflections persisted with undiminished intensity upon annealing for 40 h at 1,600 °C, confirming the equilibrium (or at least kinetically stable) composition as a mixture of the perovskite with a minority second phase.

The estimated lattice parameters of the solid solution and theoretical density values are presented in Table 1, while the lattice volume is depicted as a function of composition in Fig. 2a. The lattice volume decreases in accordance with Vegard's law up to 20 mol% substitution, as expected on substituting Ga ($^{VI}r^{3+}_{Ga} = 0.760$ Å [12]) for the smaller Al^{3+} cation ($^{VI}r^{3+}_{Al} = 0.675$ Å [12]), indicating a solubility limit for Al of about 20 mol%. For higher Al contents, where diffraction maxima corresponding to unidentified secondary phases become more intense, there is a clear deviation from linearity.

Structural data reported here are in fair agreement with literature values for similar compositions with lower aluminium contents ($x \leq 0.20$). Major discrepancies arise, however, with respect to the level of aluminium solubility in $(La,Sr)(Ga,Mg,Al)O_{3-\delta}$. Both thermodynamic calculations and experiment indicate that a complete $LaGaO_3$–$LaAlO_3$ solid solution should be attained [11] (we note that strontium and magnesium co-substitution should not have a large effect

Table 1 Lattice parameters for $La_{0.95}Sr_{0.05}Ga_{0.90-x}Al_xMg_{0.10}O_{2.925}$ indexed in space group Pnma and estimated theoretical density

x	Lattice parameters/Å			d/(g cm^{-3})
	a	b	c	
0	5.5386 (4)	7.8035 (6)	5.5026 (4)	6.94
0.05	5.5318 (1)	7.7888 (2)	5.4953 (1)	6.91
0.10	5.5262 (1)	7.7802 (2)	5.4894 (1)	6.87
0.15	5.5183 (1)	7.7699 (2)	5.4823 (1)	6.84
0.20	5.50919 (7)	7.7613 (1)	5.47467 (8)	6.80

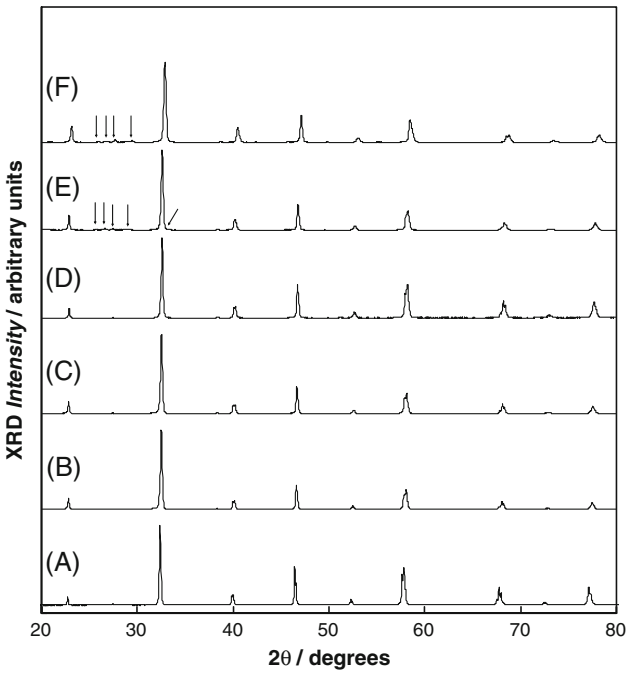

Fig. 1 Powder XRD patterns for $La_{0.95}Sr_{0.05}Ga_{0.9-x}Mg_{0.1}O_{3-\delta}$. *A* $x = 0$, *B* $x = 0.05$, *C* $x = 0.10$, *D* $x = 0.15$, *E* $x = 0.20$, *F* $x = 0.30$. *Arrows* indicate impurity phase

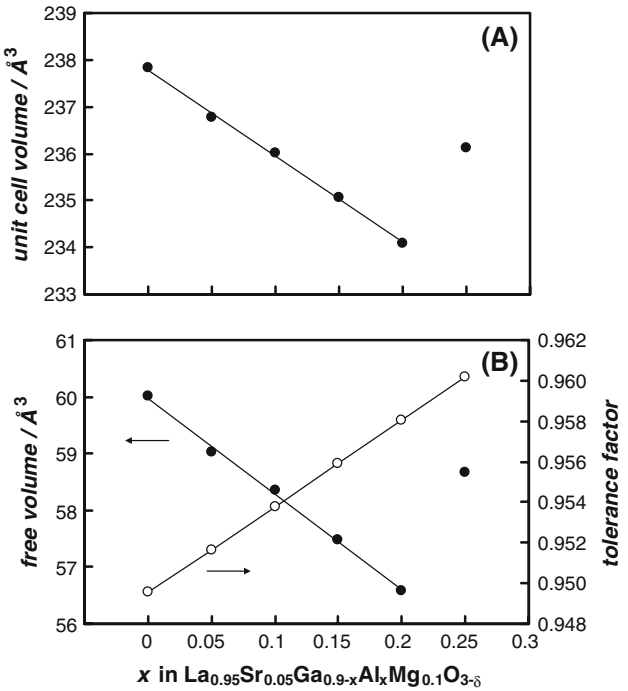

Fig. 2 **a** Unit cell volume, **b** free volume and Goldschmidt tolerance factor

on the thermodynamic properties of the system [11]). Accordingly, higher Al contents than those reported here have been obtained in the series, $La_{0.9}Sr_{0.1}Ga_{0.9-x}Al_xMg_{0.1}O_{3-\delta}$ ($0 \leq x \leq 0.8$) (although with traces of secondary phases for $x = 0$ and $x = 0.8$) [7], $La_{0.9}Sr_{0.1}Ga_{0.8-x}Al_xMg_{0.2}O_{3-\delta}$ ($0 \leq x \leq 0.3$) [11] and $LaGa_{0.9-x}Al_xMg_{0.1}O_{3-\delta}$ ($0 \leq x \leq 1$) [7]. In contrast to the conventional ceramic synthesis route used in this work, however, the three referenced reports employ wet methods of citric-acid combustion, sol–gel and spray-frozen/freeze-drying, which are known to be considerably more rapid than solid-state reaction in reaching the thermodynamic phase equilibrium. On the other hand, Sora et al. reported the formation of a mixture of two different solid solutions, one of which is based on the host $La_{0.8}Sr_{0.2}Ga_{0.8}Mg_{0.2}O_{3-\delta}$ material, $(La_{0.8}Sr_{0.2})(Ga_{1-x-y}Al_xMg_y)O_{3-\delta}$, and the other on the impurity $LaSrGa_3O_7$ ($La_{0.8}Sr_{0.2}Ga_{1-x}Al_xO_{3-\delta}$), which was present in significant quantity in their commercial carbonaceous precursor [8]. The final Al-doped material was obtained in this case following a conventional temperature-activated solid-state reaction. The presence of secondary phases, resulting from different processing protocols, thus seems to limit the solubility of Al in LSGM. It is important to note for the subsequent discussion, however, that the conventional ceramic method remains efficient for lower Al contents.

The lattice free volume and the estimated tolerance factor (based on ionic radii from [12]) are shown in Fig. 2b. The less-distorted lattice of the Al-containing materials is associated with a decrease of the lattice free volume. Considering that the oxygen stoichiometry does not change with composition, an increasing tolerance factor of the perovskite indicates higher thermodynamic stability, whereas the lower free volume is consistent with lower ionic conductivity, as the space available for movement of oxide ions within the structure is decreased.

Microstructure, thermal expansion and hardness

Scanning electron microscopy (SEM) images of polished and thermally etched $La_{0.95}Sr_{0.05}Ga_{0.90-x}Mg_{0.10}Al_xO_{3-\delta}$ ceramics are shown in Fig. 3; apparent densification ratios with respect to the XRD theoretical density are presented in

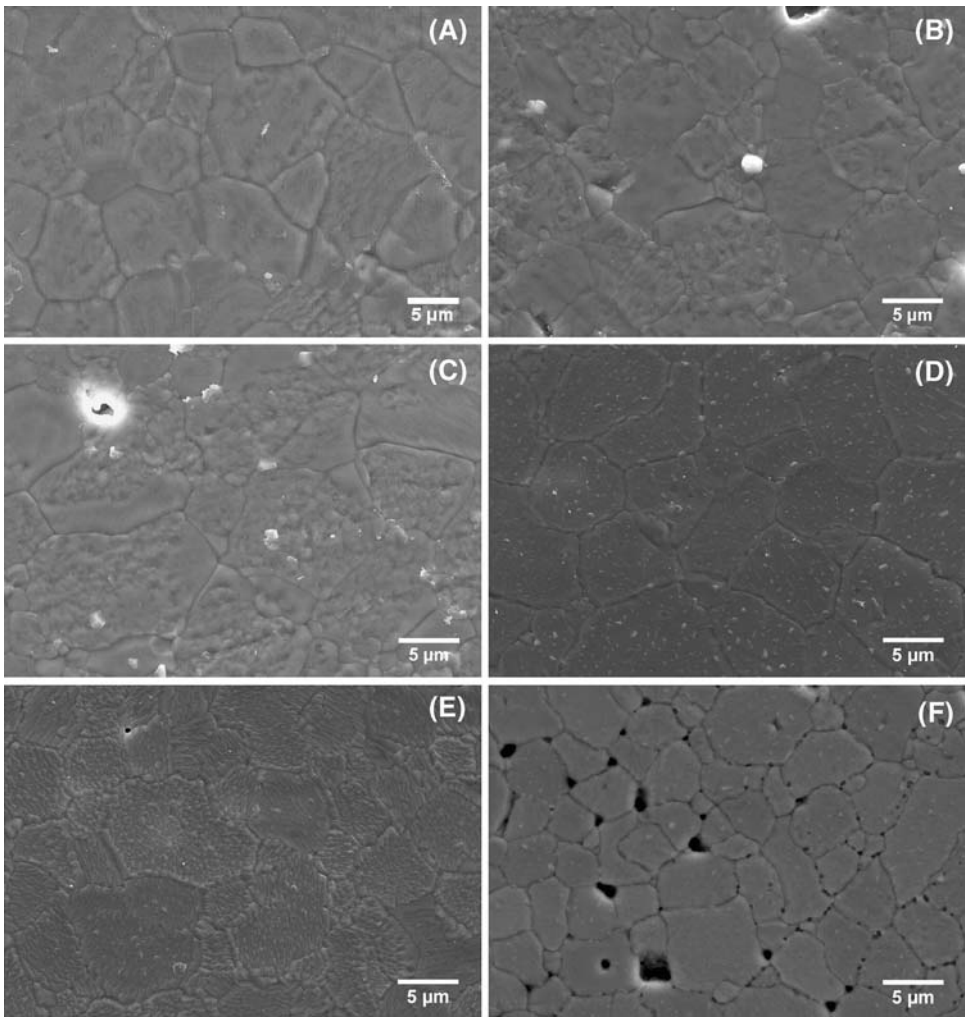

Fig. 3 SEM micrographs for (**a**) $x = 0$, (**b**) $x = 0.05$, (**c**) $x = 0.10$, (**d**) $x = 0.15$, (**e**) $x = 0.20$ and (**f**) $x = 0.30$. The scale bar is 5 μm

Table 2 Average grain size (G_{av}), fractional density (% D), linear thermal expansion coefficient (α) and Vickers hardness number (HV) measured for $La_{0.95}Sr_{0.05}Ga_{0.90-x}Al_xMg_{0.10}O_{2.925}$ ceramics

x	G_{av}/υm	% D	$\alpha/10^{-6}$ K	log[HV/(kgf^{-1} mm^2)]
0	10.9	94	11.8	5.0
0.05	9.3	94	12.4	5.2
0.10	9.8	93	11.6	4.7
0.15	10.9	93	13.5	2.8
0.20	8.0	92	12.2	2.9
0.25	5.7	>90	12.1	2.8
0.30	5.8	>90	11.9	2.9

Table 2. The 92–94% densification levels are consistent with the SEM microstructures, suggesting a slight degradation of the sintering behaviour with increasing Al content. This has been associated with inhibition of grain growth for $x \geq 0.20$ by Nguyen and Dokiya [7]. The existence of second phases could only be observed for compositions $x = 0.25$ and 0.3, residing along grain boundaries as small, Mg-rich, dark particulates, as revealed by energy dispersion spectroscopy (EDS) analysis. This suggests a decrease of Mg solubility for Al contents higher than 20 mol%, which has not been noted previously in the literature. It is highly probable that these grain-boundary secondary phases correspond to the unidentified XRD diffraction maxima observed for $x \geq 0.2$ (Fig. 1), although it is not possible to establish definite proof of a correlation at present.

The thermal expansion coefficients (α) are within the range 11.6–13.5 $\times 10^{-6}$ K^{-1} (Table 2). Slightly lower values, within a smaller range (10.5–11.3 $\times 10^{-6}$ K^{-1}), were reported for the series of $La_{0.9}Sr_{0.1}Ga_{0.90-x}Al_xMg_{0.9}O_{3-\delta}$ compositions, with $x < 0.8$ [7]. It is interesting to note that, in spite of the small α changes, both sets of data in the $0 \leq x \leq 0.3$ range exhibit a maximum in α for $x \approx 0.15$. The same authors report a consistent increase of α with increasing x for higher aluminium concentration ($0.3 < x \leq 0.8$). The nearly invariant thermal expansion, which is essentially a bulk-controlled behaviour, supports the conclusion that no significant structural or stoichiometry changes occur with increasing Al content.

Conversely, a noticeable alteration of the mechanical properties of the ceramics upon Al substitution was apparent. Vickers hardness measurements revealed an appreciable decrease in Vickers numbers (HV) for $x \geq 0.15$ (Table 2). Since the mechanical properties are, for compositionally similar materials, strongly dependent on grain boundaries, the cause of the observed decrease in HV is very likely related to the degradation of intergranular properties. This may, in turn, be associated with the coincident segregation of poorly crystallized, Mg-rich secondary phases for $x > 0.20$ (see above).

Impedance spectroscopy and ionic conductivity

In summary, the combined XRD, dilatometry, SEM and Vickers hardness analyses are all consistent with a change in the intergranular composition for aluminium contents higher than about 15 mol%, with observable impact on the microstructure and mechanical properties. The present electrical conductivity measurements reflect those compositionally controlled changes with greater sensitivity.

The impedance spectra collected in the low-temperature range (250–500 °C) present two well-resolved contributions (Fig. 4). The capacitance values estimated from the fitting results over the 250–500 °C temperature range, where the fit was possible (see "Experimental" section for calculation details), were found to be only marginally affected by composition and temperature. All values fall within the range 1×10^{-11}–2×10^{-11} F ($5 \times 10^{-11} \leq Q \leq 7 \times 10^{-11}$, $0.89 \leq n \leq 0.92$) for the high-frequency semicircle, and 9×10^{-9}–1×10^{-8} F ($5 \times 10^{-8} \leq Q \leq 10^{-7}$, $0.82 \leq n \leq 0.85$) for the low-frequency one, consistent with bulk and grain-boundary phenomena, respectively; these capacities are in good agreement with those previously reported [13].

A visual inspection of the spectra shows that the amplitude of the bulk semicircle goes through a minimum for $x = 0.10$–0.15. Further Al doping reverses the trend and the resistance recovers to the value of the Al-free material for $x = 0.3$. The grain-boundary semicircle behaves similarly, but with a minimum for $x = 0.05$, after which a substantial increase of the grain-boundary resistance with increasing aluminium content is observed. This trend is possibly due to the formation of resistive secondary

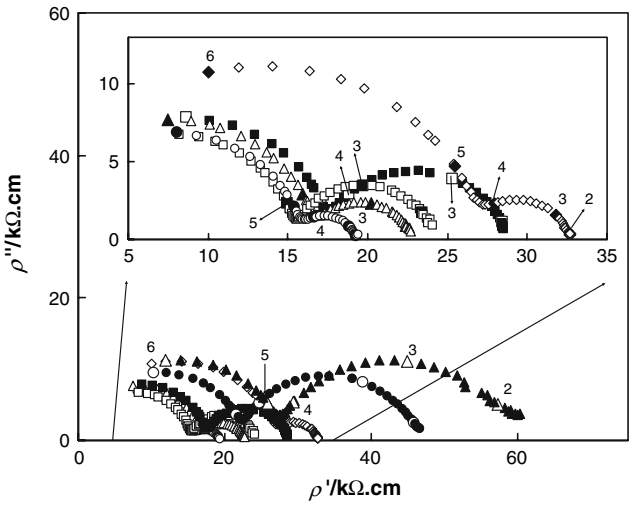

Fig. 4 Impedance spectra collected in air at 573 K: (*open diamond*) $x = 0$, (*open circle*) $x = 0.05$, (*open triangle*) $x = 0.10$, (*open square*) $x = 0.15$, (*filled square*) $x = 0.20$, (*filled circle*) $x = 0.25$, (*filled triangle*) $x = 0.30$). Numbers indicate $\log_{10}$ of frequency/Hz

phases along grain boundaries. The changes in the grain-boundary contribution are also apparent in the frequency distribution, where the peak frequency is shifted to lower values with increasing x.

The observed trends are consistently present in spectra collected for temperatures up to ca. 525°C. The temperature dependencies of both bulk and grain-boundary contributions were successfully fitted to an Arrhenius equation, as shown in Fig. 5. The activation energies for the bulk ($E_{a,b}$) and grain-boundary ($E_{a,gb}$) conductivities are given in (Table 3). The values are in good agreement with the literature, and, as is usually the case for LSGM and other solid electrolytes, $E_{a,gb}$ is slightly higher than $E_{a,b}$ [13, 14]. The effect of composition is noticed for $x \geq 0.20$ as a slight decrease of both $E_{a,b}$ and $E_{a,gb}$ with increasing Al content.

The grain-boundary conductivity values presented in Fig. 5b are estimated assuming the total surface area (S) and thickness (L) of the pellet, which is different from the microscopic grain-boundary geometric factor G_{av}/δ_{gb}, where G_{av} is an average grain size and δ_{gb} is the grain-boundary thickness. While G_{av} may be directly obtained from SEM micrographs (Fig. 3; Table 2), the determination

Table 3 Activation energy estimated for grain ($E_{a,g}$), grain-boundary ($E_{a,gb}$) and total conductivity ($E_{a,t}^{LT}$ in $T = 523$–798 K, $E_{a,t}^{HT}$ in $T = 973$–1173 K), and p-type electronic conductivity ($E_{a,ele}$)

x	$E_{a,b}$	$E_{a,gb}$	$E_{a,t}^{LT}$	$E_{a,t}^{HT}$	$E_{a,ele}$
0	0.99	1.07	1.00	0.56	1.74
0.05	0.99	1.06	0.99	0.53	1.65
0.10	0.99	1.04	0.99	0.75	1.73
0.15	0.93	1.06	0.97	0.75	1.92
0.20	0.90	1.03	0.93	0.77	1.87
0.25	0.89	0.98	0.93	0.71	2.00
0.30	0.89	0.98	0.93	0.72	1.96

Values in eV

of δ_{gb} is not straightforward. Considering the simplified brick-layer model description of a polycrystalline ceramic with large average grain size (parallel grain boundaries neglected), and assuming similar dielectric constants for the bulk and grain boundary, the grain-boundary thickness may be approximated to $\delta_{gb} = G_{av}C_b/C_{gb}$. The microscopic (or effective) grain-boundary conductivity (σ_{gb}^{mic}) is thus given by $\sigma_{gb}^{mic} = \sigma_{gb}\delta_{gb}/G_{av}$ [13, 14, 16]. The grain-boundary thickness shows a slight tendency to increase with increasing Al concentration for $x \leq 0.20$ (from 11 to 13 nm), then exhibits a much steeper increase to about 20 nm for higher Al concentrations. This step change suggests a significant modification of the grain-boundary properties for $x > 0.20$, possibly due to Al segregation, in agreement with aforementioned structural and microstructural information. This is also clearly reflected in the lower σ_{gb}^{mic} estimates obtained for the more Al-rich compositions

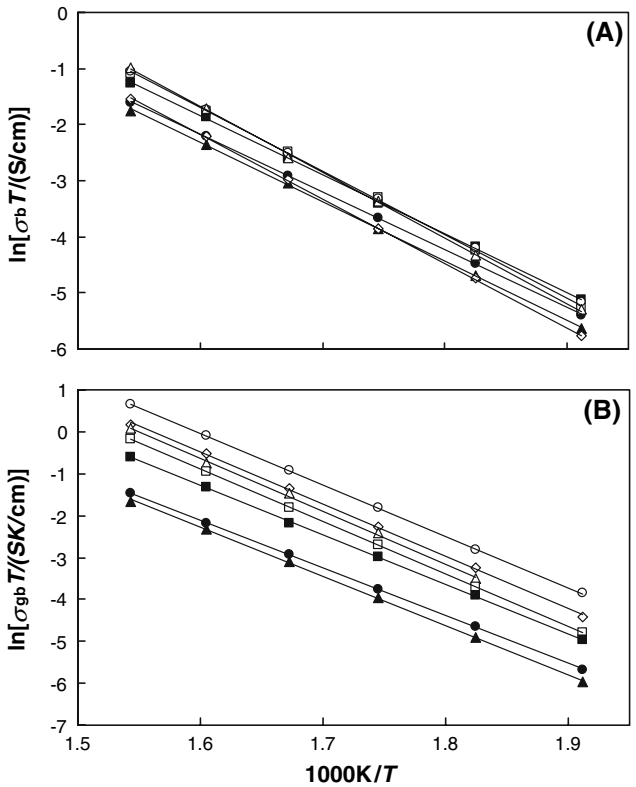

Fig. 5 Arrhenius plots for (**a**) bulk and (**b**) apparent grain boundary conductivity of $La_{0.95}Sr_{0.05}Ga_{0.9-x}Al_xMg_{0.1}O_{3-\delta}$: (*open diamond*) $x = 0$, (*open circle*) $x = 0.05$, (*open triangle*) $x = 0.10$, (*open square*) $x = 0.15$, (*filled square*) $x = 0.20$, (*filled circle*) $x = 0.25$, (*filled triangle*) $x = 0.30$)

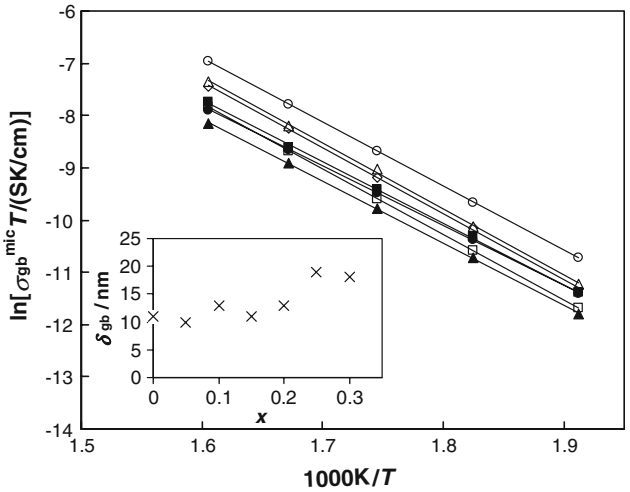

Fig. 6 The microscopic grain-boundary conductivity of $La_{0.95}Sr_{0.05}Ga_{0.9-x}Al_xMg_{0.1}O_{3-\delta}$: (*open diamond*) $x = 0$, (*open circle*) $x = 0.05$, (*open triangle*) $x = 0.10$, (*open square*) $x = 0.15$, (*filled square*) $x = 0.20$, (*filled circle*) $x = 0.25$, (*filled triangle*) $x = 0.30$. The inset shows the grain-boundary thickness

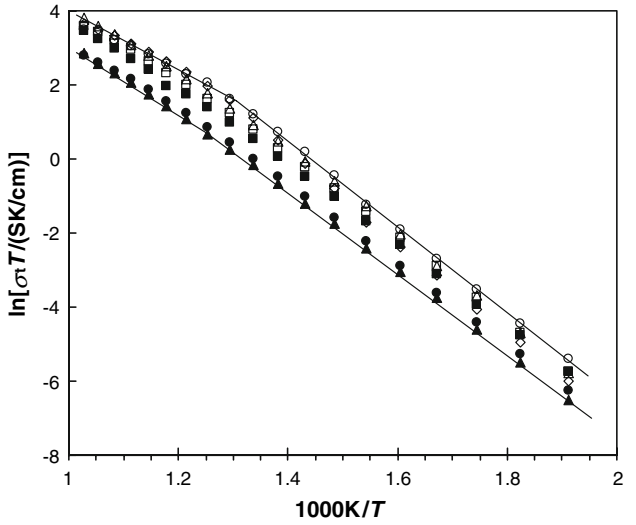

Fig. 7 Temperature dependence for the total conductivity of $La_{0.95}Sr_{0.05}Ga_{0.9-x}Al_xMg_{0.1}O_{3-\delta}$: (*open diamond*) $x = 0$, (*open circle*) $x = 0.05$, (*open triangle*) $x = 0.10$, (*open square*) $x = 0.15$, (*filled square*) $x = 0.20$, (*filled circle*) $x = 0.25$, (*filled triangle*) $x = 0.30$. Note the decrease in activation energy for $T > 500$ °C

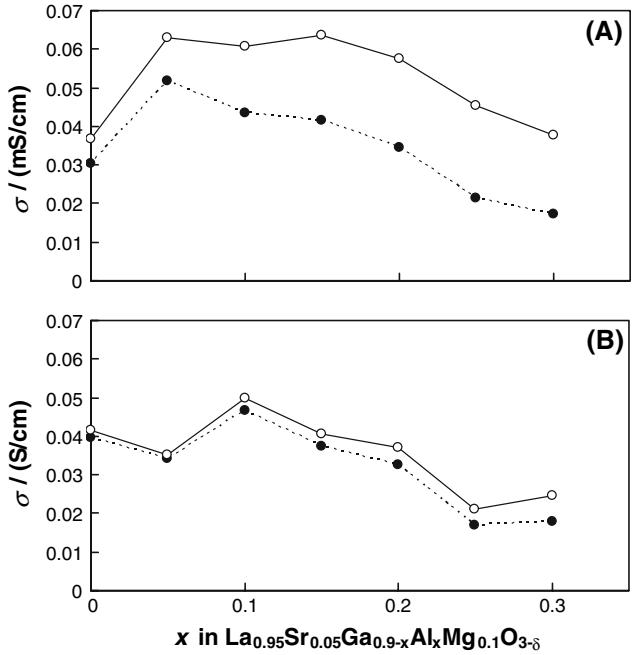

Fig. 8 Total (σ_t, *solid symbols*) and bulk (σ_b, *open symbols*) conductivity at (**a**) 300 °C and (**b**) 700 °C, plotted as a function of aluminium content

(Fig. 6), which confirm the highly resistive nature of grain boundaries in $LaGaO_3$-based materials [13, 16].

The temperature dependence of the total conductivity (σ_t) measured up to 700 °C deviates from the Arrhenius behaviour observed in the low-temperature range below ~550 °C (Fig. 7). Table 3 summarises the activation energies estimated for σ_t in the low (250–525 °C, $E_{a,t}^{LT}$), and high (550–700 °C, $E_{a,t}^{HT}$) temperature ranges, again in very good agreement with data published for $La_{0.9}Sr_{0.1}Ga_{0.90-x}Al_xMg_{0.9}O_{3-\delta}$ [7] and for $LaGa_{0.9-x}Al_xMg_{0.1}O_{3-\delta}$ [9]. Clearly, the substitution of Ga for Al increases the high-temperature activation energy for $x \geq 0.10$, thereby reducing the difference between the high- and low-temperature slopes.

Figure 8 shows the total- and bulk-conductivity values as a function of the aluminium content measured at 300 and 700 °C. At the lower temperature (Fig. 8a), the σ_t maximum for $x = 0.05$ is essentially due to an improvement of the bulk properties, and also to a slight decrease of the grain-boundary resistance. The bulk conductivity increases by more than 50% upon the introduction of 5 mol% Al. Moreover, σ_b is only marginally affected for x in the range 5–20 mol%, although the start of a trend towards lower conductivity is apparent for $x = 0.2$.

Data collected at 700 °C present considerably smaller differences in σ_t between the various materials (Fig. 8b). A maximum in σ_t is still observed (0.047 S/cm), although it is shifted to $x = 0.10$. Interestingly, the conductivity of the Al-free composition (0.041 S/cm) is very similar to that containing 20 mol% Al (0.037 S/cm). For higher Al contents ($x \geq 0.2$), σ_t decreases significantly.

Since the activation energy for σ_b is smaller than for σ_{gb}, the total conductivity should be essentially determined by the bulk properties in the high-temperature range [13, 14]. This is borne out for the Al-substituted materials presented here, as suggested by similar trends in the effect of x on σ_t at 700 °C and σ_b at 300 °C. Estimates of σ_b at the higher temperatures were thus obtained by subtracting the grain-boundary component, extrapolated from the low-temperature data, from the total resistance (Fig. 8b, open symbols). As expected, the differences between σ_t and σ_b are smaller at high temperature, although they have a tendency to increase upon Al substitution, consistent with an increasing grain-boundary resistivity with increasing Al content.

Comparison with literature data reveals two interesting aspects. First, there is a perfect match between the σ_b values depicted in Fig. 8b and those reported by Huang and co-authors [14] for the $La_{0.95}Sr_{0.05}Ga_{0.90}Mg_{0.10}O_{3-\delta}$ composition (in both cases $\sigma_b = 0.042$ S/cm at ~ 700°C). In turn, these values are similar to σ_t values in the vicinity of 0.035 S/cm measured by a dc technique for single crystals and ceramics of the same nominal composition [17]. This emphasises the consistency of data collected from different preparation and measurement methods reported by various authors.

The second, somewhat surprising aspect is that the presently reported enhancement in bulk conductivity upon substitution of Ga by a moderate fraction of Al has not been observed for nominal $La_{0.9}Sr_{0.1}Ga_{0.90-x}Al_xMg_{0.9}O_{3-\delta}$

[7] and $LaGa_{0.9-x}Al_xMg_{0.1}O_{3-\delta}$ [9], which are very similar in composition to the $La_{0.95}Sr_{0.05}Ga_{0.90-x}Al_xMg_{0.9}O_{3-\delta}$ series studied in this work. As mentioned above, differences may be related to the presence of secondary phases. According to the phase diagram published by Majewski et al. [6], which is consistent with many other literature reports, the two former compositions are outside the solid-solubility range, whereas a single-phase material is expected for the latter. This means that aluminium may be trapped by the secondary phases, thus mitigating possible effects of Al substitution on the perovskite itself.

Oxygen permeability and electronic conductivity

The observed increase in the total conductivity at high temperature may be due to an increasing contribution from p-type electronic conductivity, which predominates in lanthanum aluminate and is significantly enhanced by Sr doping [18].

Permeation measurements were carried out for all compositions in the temperature range 850–1,000 °C and in moderately oxidising conditions in order to measure the electronic conductivity. The inset of Fig. 9 shows a set of permeability data (I_0) plotted as a function of the pO_2 gradient (defined by pO_2 at permeate, p_2, and feed, p_1, sides) according to:

$$I_0 FL \Big/ RTS = \sigma_p^0 \left(P_1^{1/4} - P_2^{1/4} \right) \quad (1)$$

where σ_p^0 is the p-type electronic conductivity at unit pO_2, T is temperature, R is the gas constant, F the Faraday constant, L is the sample thickness and S the permeating area. Any significant contribution of n-type electronic conductivity is unlikely under the oxidising conditions covered in these experiments and was, therefore, neglected.

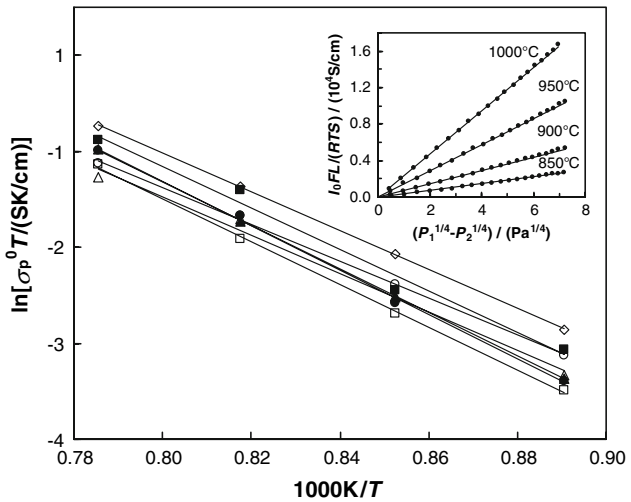

Fig. 9 Arrhenius plot of p-type electronic conductivity at unit pO_2 of $La_{0.95}Sr_{0.05}Ga_{0.9-x}Al_xMg_{0.1}O_{3-\delta}$: (*open diamond*) $x = 0$, (*open circle*) $x = 0.05$, (*open square*) $x = 0.15$, (*filled square*) $x = 0.20$, (*filled circle*) $x = 0.25$, (*filled triangle*) $x = 0.30$. Inset shows typical permeation results for $x = 0.05$ and lines show the fit to Eq. (1)

The agreement of data with Eq. (1) confirms the expectation that the permeation flux in Al-substituted LSGM is, as in the Al-free material, essentially determined by minor p-type electronic charge carriers. Surface reactions are thus not expected to play a major role on the measured flux. The estimated σ_p^0 parameters fit well to an Arrhenius law (Fig. 9). The activation energy values are quite high, in the range 1.6–2 eV (Table 3). It is apparent that σ_p^0 decreases with the addition of aluminium, although an increase in σ_p^0 with increasing x is observed for the Al-containing compositions. This is accompanied by an increase of the activation energy, which is particularly apparent for $x \geq 0.15$. Nonetheless, it is clear that the contribution of the electronic conductivity does not explain the enhancement of total conductivity for moderate concentrations of Al substitution, which, instead, is likely to result from an increase in the ionic contribution.

Effect of aluminium on the bulk conductivity

While the degradation of the electrical properties of Al-substituted LSGM seems to be largely dictated by the presence of resistive secondary phases at the grain boundaries, the underlying reasons for the enhancement in the bulk conductivity of moderately Al-substituted materials are not clear. Several possible mechanisms, all structurally dependent, may be proposed from what is known about the behaviour of unsubstituted LSGM.

As is the case for many fast oxide-ion conductors, the temperature dependence of the conductivity displays a non-Arrhenius behaviour characterised by a smooth decrease in the activation energy with increasing temperature (typically above 600–700 °C, depending on the material). Following interpretations of the same trend observed in acceptor-doped, fluorite-type oxides (ZrO_2 [19], CeO_2 [20]), Huang et al. [14] suggested that the dopant cations (Sr^{2+} and Mg^{2+}) could act as traps for oxygen vacancies $V_O^{\cdot\cdot}$ at lower temperatures. Complex, ordered vacancy clusters thus form at lower temperatures, but then progressively dissociate with increasing temperature. In the low-temperature range, the activation energy results from additive migration and association enthalpic contributions, whereas at higher temperature, defects will dissociate and the corresponding association-enthalpy term decreases. These authors [14] estimated the association enthalpy as the difference between the high- and low-temperature activation energy for the bulk conductivity, and verified that it increases significantly on increasing the Mg fraction, whereas the Sr content is less influential in trapping oxygen

vacancies. The authors thus concluded that vacancy ordering is most probably related to the association of the dopant ion Mg'_{Ga} and $V^{\cdot\cdot}_{O}$ into defect associates, e.g. $(V_OMg_{Ga})^{\cdot}$ or $(Mg_{Ga}V_OMg_{Ga})^{\times}$. This hypothesis is supported by atomistic simulation, which determined large, negative binding energies of –0.90 and –1.22 eV for $(V_OMg_{Ga})^{\cdot}$ and $(Mg_{Ga}V_OMg_{Ga})^{\times}$ defect clusters, respectively, whereas near-zero values were found for $(V_OSr_{Ga})^{\cdot}$ and $(Sr_{Ga}V_OSr_{Ga})^{\times}$ [21]. It should be noted that, given the extraordinarily high defect concentration in such materials, it is unlikely that oxygen vacancies can persist without any type of interaction with other defects even at high temperature. Simple defect association-dissociation models are, from this perspective, clearly limited.

Huang et al. report an association enthalpy of 0.32 eV for $La_{0.95}Sr_{0.05}Ga_{0.90}Mg_{0.10}O_{3-\delta}$, which is slightly lower than that of 0.43 eV estimated in this work from the values of $E_{a,b} - E^{HT}_{a,t}$ (see Table 1). In the case of $La_{0.95}Sr_{0.05}Ga_{0.90-x}Al_xMg_{0.10}O_{3-\delta}$, the decrease of $E_{a,b} - E^{HT}_{a,t}$ for $x \geq 0.10$ suggests that the Al^{3+} cations may serve to increase the fraction of free (unassociated) $V^{\cdot\cdot}_{O}$. Since the total $[V^{\cdot\cdot}_{O}]$ remains constant with x, this provides a possible explanation for the enhanced ionic conductivity observed for $x = 0.10$. In the low-temperature range, the slight decrease in the bulk-conductivity activation energy ($E_{a,b}$) is consistent with the hypothesis of increased disorder upon Al substitution.

Haavik et al. [13] have attempted to model the high-temperature, non-Arrhenius behaviour of LSGM, assuming the formation of $(V_OMg_{Ga})^{\cdot}$ defect clusters. The model successfully fitted data for $La_{0.90}Sr_{0.10}Ga_{0.90}Mg_{0.10}O_{3-\delta}$ with an association enthalpy of 0.83 eV. The fit was clearly poorer, although still acceptable, for $La_{0.95}Sr_{0.05}Ga_{0.95}Mg_{0.05}O_{3-\delta}$, but the model proved inadequate for the low-temperature region of $La_{0.99}Sr_{0.01}Ga_{0.99}Mg_{0.01}O_{3-\delta}$, leading to the conclusion that the enthalpy and entropy of association depend strongly on composition. The association enthalpy of 0.83 eV agrees well with the atomistic-simulation calculations of Islam and Davies mentioned above [21]. However, this value appears excessively large when compared to the estimate of Huang et al. for the same compositions (0.14 and 0.26 eV); it also appears rather large on considering that the activation energy of ionic conductivity in the low-temperature range is $\sim$1 eV.

Alternatively, the low-temperature dependence of the bulk-relaxation phenomena may be analysed in order to obtain estimates of oxide-ion migration and defect-association enthalpies, E_{mig} and E_{ass}, respectively [17]. Figure 10a depicts the typical frequency dependency of the loss tangent (tanδ) for $La_{0.95}Sr_{0.05}Ga_{0.90-x}Al_xMg_{0.10}O_{3-\delta}$ at 250 °C. Analogous to the impedance spectra, where two semicircles are apparent, two tanδ-maxima (tanδ_{max}), occurring at the resonance frequency $f_{tan\delta}$, denote bulk and grain-boundary relaxation phenomena. Following the approximation suggested by Kurumada et al. [17], the proportionality relations $f_{tan\delta} \propto \exp(-E_{mig}/RT)$ and $\tan\delta_{max} \propto \exp(-E_{ass}/RT)/T$ represent Arrhenius dependencies with slopes determined by the migration and association enthalpies. These relations, plotted in Arrhenius form in Fig. 10b and c do indeed show a high degree of linearity within a temperature range from 250 to 300–350 °C, where the materials are expected to retain orthorhombic symmetry. Data deviate from linearity at higher temperatures (not shown) probably due to the orthorhombic → monoclinic phase transition that occurs at $\sim$300 °C [22].

One additional note should be made about the magnitude of the values of $f_{tan\delta}$ and tanδ_{max}. According to the brick-layer model, $f_{tan\delta}$ and tanδ_{max} may be affected by microstructural features (e.g. grain size, segregation of secondary phases) which determine the ratio between the

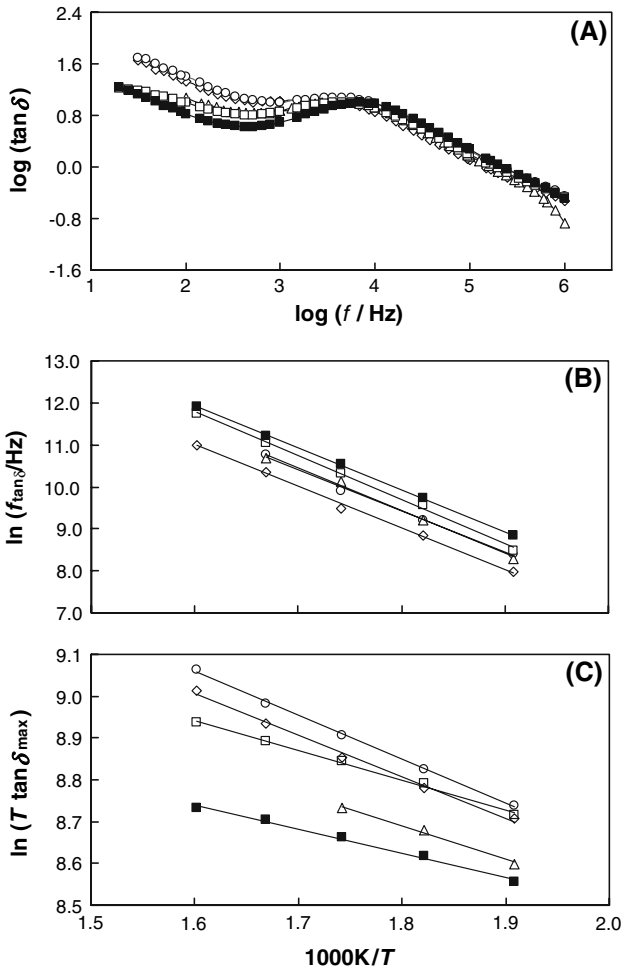

Fig. 10 (**a**) Frequency dependence of tanδ and temperature dependence of (**b**) tanδ_{max} frequency and of (**c**) tanδ_{max}: (*open diamond*) $x = 0$, (*open circle*) $x = 0.05$, (*open diamond*) $x = 0.10$, (*open square*) $x = 0.15$, (*filled square*) $x = 0.20$

bulk and grain-boundary resistances, R_{gb}/R_b. In fact, analytical expressions may be derived showing that $f_{\tan\delta}$ increases with increasing R_{gb}/R_b, whereas the opposite trend is expected for $\tan\delta_{max}$ [23]. This is indeed what is represented by Fig. 10. Nevertheless, according to the same model, the $f_{\tan\delta}$ and $\tan\delta_{max}$ temperature dependencies do not change with microstructure; thus, meaningful values of E_{mig} and E_{ass} may be obtained.

The E_{mig} and E_{ass} estimated on the basis of this model are shown in Fig. 11 as a function of the aluminium content. It can be seen that the association enthalpy decreases for $x \geq 0.10$, as found from the difference of $E_{a,b} - E_{a,t}^{HT}$ (suggested by Huang et al. [14]), but the magnitude of the values is about 20–30% lower in the case of the estimated results. Both values are much lower than the range of 0.8–0.9 eV, which was both calculated [21] and derived [13] assuming the formation of simple $(V_O Mg_{Ga})^{\cdot}$ defect clusters. This may indicate that a more complex defect chemistry is involved, at least for the less-substituted compositions. Interestingly, measurements of formation enthalpies by oxide-melt-solution and differential-scanning calorimetries of LSGM materials with different oxygen stoichiometries suggest that the enthalpy of any order-disorder transition occurring between room temperature and 700 °C should be very small (of the order of 0.01 eV or less) [24]. This is in agreement with ab initio calculations of the enthalpy changes for the orthorhombic → rhombohedral phase transition in $LaGaO_3$ [25], also consistent with low association enthalpies.

In turn, the migration term E_{mig} is little affected by composition, although it tends to increase with increasing x up to 0.15. A value of 0.85 eV, significantly higher than that derived from the high-temperature region of the Arrhenius plot (0.56 eV), was estimated for $La_{0.95}Sr_{0.05}Ga_{0.90}Mg_{0.10}O_{3-\delta}$. Nevertheless, the summation of the migration and association terms, $E_{mig} + E_{ass}$, is in good agreement with the activation energy for the bulk ionic conductivity, $E_{a,b}$. This may be seen as supporting the coherence of this alternative interpretation of the low-temperature impedance spectra (Fig. 11).

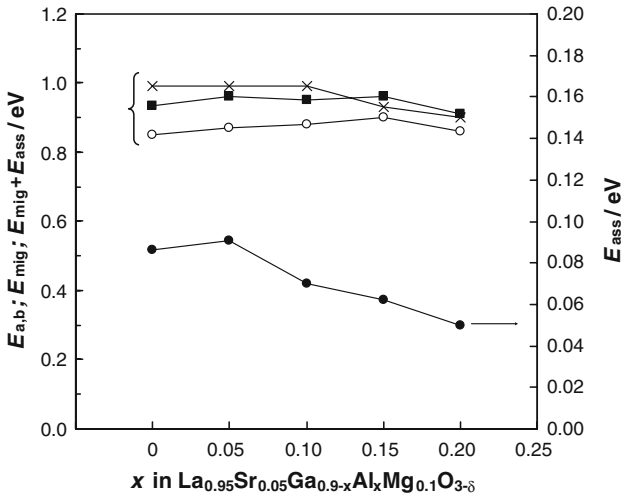

Fig. 11 Activation energies for oxide-ion migration (E_{mig}), oxygen-vacancy association (E_{ass}) and bulk conductivity ($E_{a,b}$) plotted as a function of the aluminium content (*cross* $E_{a,b}$, *open circle* E_{mig}, filled circle E_{ass}, filled square $E_{mig} + E_{ass}$)

One obvious consequence of this rationale is that the order–disorder transition does not fully account for the non-Arrhenius behaviour in LSGM, in particular the larger activation energy measured in the low-temperature region. Some authors have suggested that the curvature in the Arrhenius plots could be due to a transition to a higher-symmetry structure at high temperature, which is more conductive than the low-temperature phase. For the composition $La_{0.90}Sr_{0.10}Ga_{0.80}Mg_{0.20}O_{3-\delta}$, a transition from monoclinic to rhombohedral symmetry was reported to occur at 500–750 °C due to a lowering of the $(Ga,Mg)O_6$ octahedra tilt angle [26, 27]. Very similar structural behaviour is observed for $La_{0.95}Sr_{0.05}Ga_{0.90}Mg_{0.10}O_{3-\delta}$. After the above-mentioned orthorhombic → monoclinic transition at ~300 °C, the symmetry changes to rhombohedral ($I2/a \rightarrow R3c/R\bar{3}c$) at ~500 °C/~600 °C [22]. The apparent correlation between the phase-transition temperature and that of the non-Arrhenius curvature suggested that this could be the reason for the lower migration enthalpy, as an alternative argument to the order-disorder transition model. However, as noted by Haavik et al. [13] and Skowron et al. [28], it is unlikely that the minor structural differences between the low- and high-temperature phases (a decrease in the $(Ga,Mg)O_6$ octahedral tilting) could be responsible for such a significant difference in the migration enthalpy. In fact, calculated migration enthalpies (0.64–0.73 eV) for oxygen vacancies along GaO_6 octahedral edges in pseudo-cubic and orthorhombic $LaGaO_3$ are not very different and are well below 1 eV [29, 30]. The same argument can hardly explain the trends observed for the aluminium-substituted materials, although a less-distorted structure is to be expected (Fig. 1b).

However, the coincident temperature range of the phase-transition and the deviation from non-Arrhenius behaviour do suggest some correlation. As for many other perovskites, e.g. $LaAlO_3$ [30] and $CaTiO_3$ [32], widespread twinning of domains has been observed in LSGM materials due to the formation of ferroelastic domain boundaries, resulting from an increased degree of tilting of $(Ga,Mg)O_6$ octahedra upon cooling [33, 34].

Atomistic simulations of the model perovskite, $CaTiO_3$, suggest that the ferroelastic domain walls are energetically favourable sites for the location of oxygen vacancies [32]. The domain walls are, thus, likely to display greater ionic conductivity than the bulk (as for WO_3 [35]). These

domain walls may be extremely mobile, if mobile defects such as oxygen vacancies are present. It is perhaps interesting to note that an activation energy of the order of 0.89–0.98 eV (25–300 °C) was determined for domain-wall motion in $LaAlO_3$ [36], values which are similar to the activation energy measured for the oxide-ionic conductivity (1.05–1.15 eV [37, 38]. Domain-wall motion has thus been attributed to the diffusion of oxygen vacancies.

Transmission electron microscopy of $La_{0.80}Sr_{0.20}Ga_{0.85}Mg_{0.15}O_{3-\delta}$ revealed a temperature-reversible, twinned microstructure which is stable up to $\sim$500 °C. It was suggested that these twin boundaries separate domains of randomly spaced, planar clusters of oxygen vacancies [28]. This may indicate that highly mobile vacancies (and the dopants) are concentrated in the vicinity of the domain walls, forming an additional fast oxygen-diffusion path that may significantly contribute to increasing the total grain-bulk conductivity.

Although there is no high-temperature structural study of $La_{0.95}Sr_{0.05}Ga_{0.90-x}Al_xMg_{0.10}O_{3-\delta}$, the oxygen stoichiometry and the average structure do not change with Al substitution, at least for $x \leq 0.20$. The displacive phase transitions leading to the ferroelastic domains should, therefore, be similar and occur at the same temperature for the Al-containing range of compositions as for Al-free LSGM. The hypothesis of additional parallel oxygen-migration paths along domain walls may thus explain a value for E_{mig} of the order of 0.85–0.9 eV in the low-temperature region. On the other hand, the increase in bulk ionic conductivity and the decrease of the association enthalpy observed for moderate fractions of aluminium both suggest an increase in the concentration of free oxygen vacancies in the domain walls, resulting from a lower energy required for their formation.

In the temperature range above 500–600 °C, the domain structure is broken up and ionic transport, with lower activation energy, proceeds within the perovskite matrix. In the high-temperature range, substituting Ga with Al increases $E_{a,t}^{HT}$ from 0.56 eV for $x = 0$ to 0.75 eV for $x \geq 0.10$. Such a trend may be explained as resulting from oxygen migration along paths with higher activation energy around percolating Al^{3+} cations.

Experimental

Materials preparation and characterisation

Dense ceramic samples with nominal composition $La_{0.95}Sr_{0.05}Ga_{0.90-x}Mg_{0.10}Al_xO_{3-\delta}$ were prepared via a conventional ceramic route starting from high-purity Al_2O_3, La_2O_3, $SrCO_3$ (Merck), Ga_2O_3 (Aldrich) and MgO (Panreac). After an initial calcination step of lanthanum and magnesium oxides (1,100 °C for 10 h) to eliminate hydroxides or carbonates, all precursors were mixed in ethanol in a planetary ball-mill, dried and calcined at 1,100 °C for 12 h, then again ball-milled and dried. The resulting powder was pressed into disk-shaped pellets and subsequently sintered at 1,600 °C during 4 h with heating and cooling rates of 5 K/min. The apparent density of ceramic samples was estimated from mass and geometry measurements.

Phase purity and completion of reaction of ground ceramics were analysed by XRD with a Rigaku Geigerflex D/Max-C series diffractometer using Cu Kα radiation. Diffraction patterns were collected at room temperature in the range $10^\circ < 2\theta < 110^\circ$, with a step-width of 0.02° and a collection time of 10 s per point. The title phases were indexed in space group Pnma, analogous to similar LSGM compositions with orthorhombic symmetry [7, 9, 11]. Lattice parameters were determined by Rietveld refinement of the corresponding structural model using the program FULLPROF [39].

Ceramic samples were polished down to 0.25 μm with diamond paste and thermally etched at 1,500 °C for 30 min for analyses by SEM and energy dispersive X-ray spectrometry (EDS) using a Hitachi 4100S microscope equipped with an EDS Röntec detector. The SEM micrographs were analysed using the linear-intercept method to obtain estimates of the average grain-equivalent diameter (G_{av}) [40, 41].

The thermal-expansion behaviour of sintered, prismatic, dense ceramic samples (15 mm long and square section) was evaluated in air over the temperature range from 25 to 1,100 °C in a Netzsch 402EL dilatometer with a heating rate of 10 K/min. The linear thermal-expansion coefficient (α) was averaged over the linear part of the dilatometric plots assuming $\alpha = \Delta L/\Delta T/L_0$, where L is the sample length at a given temperature and L_0 the initial length of the sample.

The hardness of ceramic samples was measured following the Vickers method using a Shimadzu mechanical indenter. Vickers numbers (*HV*) were obtained after applying a load for 15 s and the actual result is an average of six independent measurements.

Impedance spectroscopy

The electrical properties of the ceramic samples were studied by impedance spectroscopy in air between 250 and 900 °C. The spectra were collected in the frequency range 20–10^6 Hz with $V_{ac} = 100$ mV using a Hewlett Packard 4284A impedance analyser. Platinum (Engelhard) electrodes were painted onto both pellet surfaces and fired at 1,000 °C for 5 min to provide the necessary electrical contacts.

The impedance spectra were fitted to an equivalent circuit consisting of a series association of two elements described by a resistance (R_j) in parallel with a constant phase element (CPE_j) of impedance $Z_{CPE} = 1/[(iw)^n Q]$, where Q is a pseudocapacitance and n an exponent. This circuit may be described using Boukamp's notation as $(R_bQ_b)(R_{gb}Q_{gb})$, where the subscripts denote the grain bulk and the grain boundary; the total resistance is simply obtained through $R_t = R_b + R_{gb}$. As temperature increases, the circuit is first simplified to $R_b(R_{gb}Q_{gb})$ and, for higher temperatures, when spectra consist only of the electrode contribution, the R_t values are taken as the high-frequency intercept with the real axis. The fitting parameters for both bulk and grain-boundary semicircles include, besides the resistances and the pseudo-capacitances (Q_b, Q_{gb}), the coefficients n_b and n_{gb}. These parameters account for the depression of the semicircles and are combined with Q in order to estimate the true capacitances, $C_j = R_j^{(1-n)/n} Q_j^{1/n}$. The electrical conductivities were estimated by the general relation $\sigma_j = R_j L/S$ (j = b, gb or t identify the bulk, grain boundary and total conductivity contributions), where L is the sample thickness and S the surface area of the electrodes. The equivalent circuit analysis was carried out with dedicated codes, either Equivalent Circuit (Version 3.97, 1989, B. Boukamp) or ZView (Version 2.6b, 1990–2002, Scribner Associates).

Oxygen permeability

Oxygen-permeability measurements were carried out using an electrochemical cell consisting of a YSZ disk (diameter 18 mm, thickness 2 mm) with two sets of platinum electrodes, placed at 4 mm from each other, on each face of the disk on an engraved area of 10 mm in diameter and 1 mm in thickness. The measured sample was sealed with an appropriate glass on top of the YSZ disk forming a closed chamber, as described in Ref. [42]. The smaller electrodes serve as a Nernstian probe to monitor the oxygen partial pressure (pO_2) inside the chamber (P_2), and the larger ones are connected to a DC source to work as an oxygen electrochemical pump driving oxygen out and thus creating a pO_2 gradient across the membrane. The pO_2 at the outer membrane surface (P_1) was determined by atmospheric air. Under steady state, the pumping current (I_{pump}) is compensated by the permeation current through the sample ($I_0 = I_{pump}$). The underlying relations and additional experimental details, including detection of leaks through glass seals and the gas impermeability of the samples, may be found in Ref. [43]. Measurements performed on samples with different thickness yielded virtually identical results (within <2%), which are a clear indication that the permeation flux is determined by the bulk transport properties, and not by slow surface reaction kinetics.

Acknowledgments The authors express their gratitude for financial support from COST Action 525, PRODEP (E. Gomes), FCT (Portugal), and CEC-Brussels (NoE FAME).

References

1. Ishihara T, Matsuda H, Takita Y (1994) J Am Chem Soc 116:3801
2. Feng M, Goodenough JB (1994) Eur J Solid State Inorg Chem 31:663
3. Huang P, Petric A (1996) J Electrochem Soc 143:1644
4. Huang K, Tichy RS, Goodenough JB (1998) J Am Ceram Soc 81:2581
5. Yamaji K, Horita T, Ishikawa M, Sakai N, Yokokawa H (1998) Solid State Ion 108:415
6. Majewski P, Rozumek M, Aldinger F (2001) J Alloys Comp 329:253
7. Nguyen TL, Dokiya M (2000) Solid State Ion 132:217
8. Sora IN, Pelosato R, Dotelli G, Schmid C, Ruffo R, Mari CM (2005) Solid State Ion 176:81
9. Kajitani M, Matsuda M, Miyake M (2007) Solid State Ion 178:355
10. Yasuda I, Matsuzaki Y, Yamakawa T, Koyama T (2000) Solid State Ion 135:381
11. Matraszek A, Miller M, Singheiser L, Hilpert K (2003) J Am Ceram Soc 86:1911
12. Shannon RD (1976) Acta Cryst A32:751
13. Haavik C, Ottesen EM, Nomura K, Kilner JA, Norby T (2004) Solid State Ion 174:233
14. Huang K, Tichy RS, Goodenough JB (1998) J Am Ceram Soc 81:2565
15. Fleig J (2000) Solid State Ion 131:117
16. Gomes E, Soares MR, Figueiredo FM, Marques FMB (2005) J Eur Ceram Soc 25:2599
17. Kurumada M, Iguchi E, Savytskii DI (2006) J Appl Phys 100:014107
18. Nguyen TL, Dokiya M, Wanga S, Tagawa H, Hashimoto T (2000) Solid State Ion 130:229
19. Suzuki Y (1995) Solid State Ion 81:211
20. Huang K, Feng M, Goodenough JB (1998) J Am Ceram Soc 81:357
21. Islam MS, Davies RA (2004) J Mat Chem 14:86
22. Vasylechko L, Vashook V, Savytskii D, Senyshyn A, Niew R, Knapp V, Ullmann V, Berkowski M, Matkovskii A, Bismayer U (2003) J Solid State Chem 172:396
23. Abrantes JCC, Coll DP, Nuñez P, Figueiredo FM, Frade JR (Submitted) On the origin of tg(δ) maxima revealed by impedance spectra. Part I: model behaviour
24. Cheng J, Navrostky A (2004) J Solid State Chem 177:126
25. Wu B, Zinkevich M, Aldinger F, Zhang W (2007) J Phys Chem Solids 68:570
26. Slater PS, Irvine JTS, Ishiara T, Takita Y (1998) J Solid State Chem 139:135
27. Yashima M, Nomura K, Kageyama H, Miyazaki Y, Chitose N, Adachi K (2003) Chem Phys Let 380:391
28. Skowron A, Huang P-N, Petric AJ (1999) J Solid State Chem 143:202
29. Khan MS, Islam MS, Bates DR (1998) J Phys Chem B 102: 3099
30. De Souza RA, Maier J (2003) Phys Chem Chem Phys 5:740
31. Bueble S, Knorr K, Brecht E, Schmahl W (1998) Surf Sci 400:345
32. Calleja M, Dove MT, Salje EKH (2003) J Phys Condens Matter 15:2301

33. Drennan J, Zelizko V, Hay D, Ciacchi FT, Rajendran S, Badwal SPS (1997) J Mater Chem 7:79
34. Savytskii DI, Trots DM, Vasylechko LO, Tamura N, Berkowski M (2003) J Appl Cryst 36:1197
35. Aird A, Salje EKH (1998) J Phys Condens Matter 10:L337
36. Harrison RJ, Redfern SAT, Salje EKH (2004) Phys Rev B 69:144101
37. Park JY, Choi GM (2002) Solid State Ion 154–155:535
38. Anderson PS, Marques FMB, Sinclair DC, West AR (1999) Solid State Ion 118:229
39. Rodriguez-Carvajal J (1990) FullProf. In: Satellite meeting on powder diffraction. Abstracts of the XVth conference on the international union of crystallography, Toulouse, p 127
40. Anderwood E (1970) Quantitative stereology. Addison-Wesley, Boston
41. Mendelson MI (1969) J Am Ceram Soc 42:443
42. Gomes E, Marques FMB, Figueiredo FM (2008) Solid State Ion 179:1325
43. Figueiredo FM, Marques FMB, Frade JR (1998) Solid State Ion 110:45